

Understanding the impact of heavy ions and tailoring the optical properties of large-area Monolayer WS₂ using Focused Ion Beam

Fahrettin Sarcan^{1,2,}, Nicola J. Fairbairn³, Panaiot Zotev⁴, Toby Severs-Millard⁴, Daniel Gillard⁴,
Xiaochen Wang⁵, Ben Conran⁵, Michael Heuken⁶, Ayse Erol²,
Alexander I. Tartakovskii⁴, Thomas F. Krauss¹, Gordon J. Hedley³, Yue Wang^{1,*}*

¹ Department of Physics, School of Physics, Engineering and Technology, University of York, York, YO10 5DD, United Kingdom

² Department of Physics, Faculty of Science, Istanbul University, Vezneciler, Istanbul, 34134, Turkey

³ School of Chemistry, University of Glasgow, Glasgow, G12 8QQ, United Kingdom

⁴ Department of Physics and Astronomy, University of Sheffield, Sheffield S3 7RH, United Kingdom

⁵ AIXTRON Ltd., Buckingway Business Park, Anderson Rd, Swavesey, Cambridge CB24 4FQ, Great Britain

⁶ AIXTRON SE, Dornkaulstraße, 52134 Herzogenrath, Germany

KEYWORDS: WS₂, focused ion beam, defect engineering, surface damage, transition metal dichalcogenides, trion emission

ABSTRACT: Focused ion beam (FIB) has been used as an effective tool for precise nanoscale fabrication. It has recently been employed to tailor defect engineering in functional nanomaterials such as two-dimensional transition metal dichalcogenides (TMDCs), providing desirable properties in TMDC-based optoelectronic devices. However, the damage caused by the FIB irradiation and milling process to these delicate atomically thin materials, especially in the extended area, has not yet been elaboratively characterised. Understanding the correlation between lateral ion beam effects and optical properties of 2D TMDCs is crucial in designing and fabricating high-performance optoelectronic devices. In this work, we investigate lateral damage in large-area monolayer WS_2 caused by the gallium focused ion beam milling process. Three distinct zones away from the milling location are identified and characterised via steady-state photoluminescence (PL) and Raman spectroscopy. An unexpected bright ring-shaped emission around the milled location has been revealed by time-resolved PL spectroscopy with high spatial resolution. Our finding opens new avenues for tailoring the optical properties of TMDCs by charge and defect engineering via focused ion beam lithography. Furthermore, our study provides evidence that while some localised damage is inevitable, distant destruction can be eliminated by reducing the ion beam current. It paves the way for the use of FIB to create nanostructures in 2D TMDCs, as well as the design and realisation of optoelectrical devices on a wafer scale.

Focused ion beam (FIB) milling is a powerful lithographic technique with nanometre resolution¹, especially when the samples can potentially be damaged by wet chemicals that are required in electron-beam or photo-lithography processes. FIB lithography is often employed as the all-dry nanofabrication method for plasmonic²⁻⁴, photonic^{5,6} and microfluidic⁷ devices, in applications such as sensors, photodetectors, and light emitters⁸⁻¹². Alongside these applications, more recently, FIB has shown great potential in surface modification and defect engineering in two-dimensional materials, especially in the transition metal dichalcogenides (TMDCs) family, with the aim to tailor their optical and electrical properties¹²⁻¹⁹. It has been shown that direct ion beam irradiation can controllably create chalcogenide and

transition metal vacancies, thus manipulating the material's stoichiometry. Ma *et al.* showed that argon ion irradiation can modify the optical properties of WS₂ monolayers (MLs). Sulphur vacancies in ML WS₂ create mid-bandgap states, resulting in enhanced saturable absorption in the near-IR wavelength region¹⁵. Furthermore, controlling the stoichiometry-based defects can also tune the conductivity of 2D materials, sometimes even resulting in a change from a metallic to insulating phase. Stanford *et al.* showed that controlling the ion irradiation dose can selectively introduce precise local defects in few-layer WSe₂, thereby locally tuning the resistivity and transport properties²⁰. Also, focused helium ion beams have been used to deterministically create defects in MoS₂, WS₂ and WSe₂²¹. With helium ion irradiation, other than the expected local defects, the sputtered chalcogenide atoms also create an extended percolating network of defects, which results in edge states throughout the monolayers. Using FIB to control defect generation in 2D materials paves the way to fabricate nanoscale novel optoelectrical devices, including single-photon emitters, memory devices, resistors, and atomically thin circuits^{9,20-22}.

While FIB is the ideal tool for high-precision nanomaterial manipulation, the main challenge is to understand the potential destruction to the materials, not only locally but also in the extended area, and discover how to minimise undesirable damage. The exceptionally delicate nature of these atomically thin 2D materials means that the lateral impact of sputtered ions and milled (and potentially redeposited) atoms becomes critical. Understanding and managing the lateral impact during the inherently destructive FIB process is key to maintaining high-performance nanodevices based on these 2D materials^{23,24}. To the best of our knowledge, there are only two studies in the literature regarding quantifying the lateral damage area of ion beam lithography on 2D materials. Both studies are based on chemical-vapor-deposited (CVD) graphene^{25,26}. It has been shown that the ions can reach a maximum lateral distance of approximately 30 μm . While Liao *et al.*²⁵ attributed this effect to the deleterious tail of unfocused ions in the ion beam probe, Thissen *et al.*²⁶ believe that sputtered gallium ions in the residual gas are the main cause of the long-distance lateral damage. To qualitatively determine the ion sputtering effect around the milled area, there are other studies of graphene that have used Raman spectroscopy to investigate the intensity ratio between

the defect-induced Raman feature (D band) and the so-called native graphene feature, G band^{27,28}. The D/G ratio of the Raman features decreased exponentially and reached a minimum value at around 15-30 μm away from the area milled by a focused gallium ion beam.

The above studies are all based on graphene. In 2D TMDCs, although the local defects introduced by the ion beam have been studied, the extended lateral impact of the ion beam milling/lithography process, especially the impact on their light-emitting properties remains unknown. In this letter, we performed focused gallium ion beam lithography on a large area monolayer WS_2 with a range of ion beam currents. We report the impact of focused gallium ions on monolayer WS_2 at different lateral locations and explore the origins of these effects.

Monolayer WS_2 was grown on a 2-inch sapphire substrate by AIXTRON Ltd. using a Close Coupled Showerhead metal organic vapour deposition reactor. The uniformity of as-grown ML WS_2 across the 2-inch wafer was assessed by photoluminescence and Raman spectroscopy. Centimetre-sized monolayers of WS_2 are transferred from the sapphire substrate onto pre-marked 300 nm SiO_2 -on-Si substrates, using a wet-transfer process with a polymethyl methacrylate (PMMA) layer as a carrier. PMMA was then removed in an acetone bath.

Figure 1b shows the PL spectrum measured from a pristine ML WS_2 on SiO_2/Si substrate, using a microPL setup²⁹. The 532 nm excitation laser beam is focused to a spot of $\sim 1.5 \mu\text{m}$ in diameter on the sample. The main PL peak energy of pristine ML WS_2 is $\sim 2.03 \text{ eV}$, which corresponds to the neutral excitonic transition^{16,30-33}, presented as A^0 in Figure 1. Over the area of interest (within a circular region from the central milled hole, with a radius up to 300 μm), the A^0 peak energy varies $\pm 4 \text{ meV}$ and the integrated intensities fluctuate by $\pm 5\%$; this fluctuation is originated from wafer-scale ML CVD growth and the wet-transfer process. Additionally, we observe PL emission at lower energies (two shoulders in Figure 1b, peaked at 1.98 eV and 1.80 eV respectively), corresponding to trions and defect-bound states in ML WS_2 ^{30,31}. The energy difference between the A^0 peak (neutral excitons) and the A^T peak (trions) is $\sim 34 \text{ meV}$, in agreement with the literature³⁰. The trions in as-grown TMDCs are attributed to native

defects and TMDC–substrate interaction^{34,35}. The lowest energy peak, defect-bound exciton peak D^S , is attributed to S-deficiency induced emission, previously discussed in the S-based TMDCs, such as MoS_2 and WS_2 ^{13–16,30–33,36}.

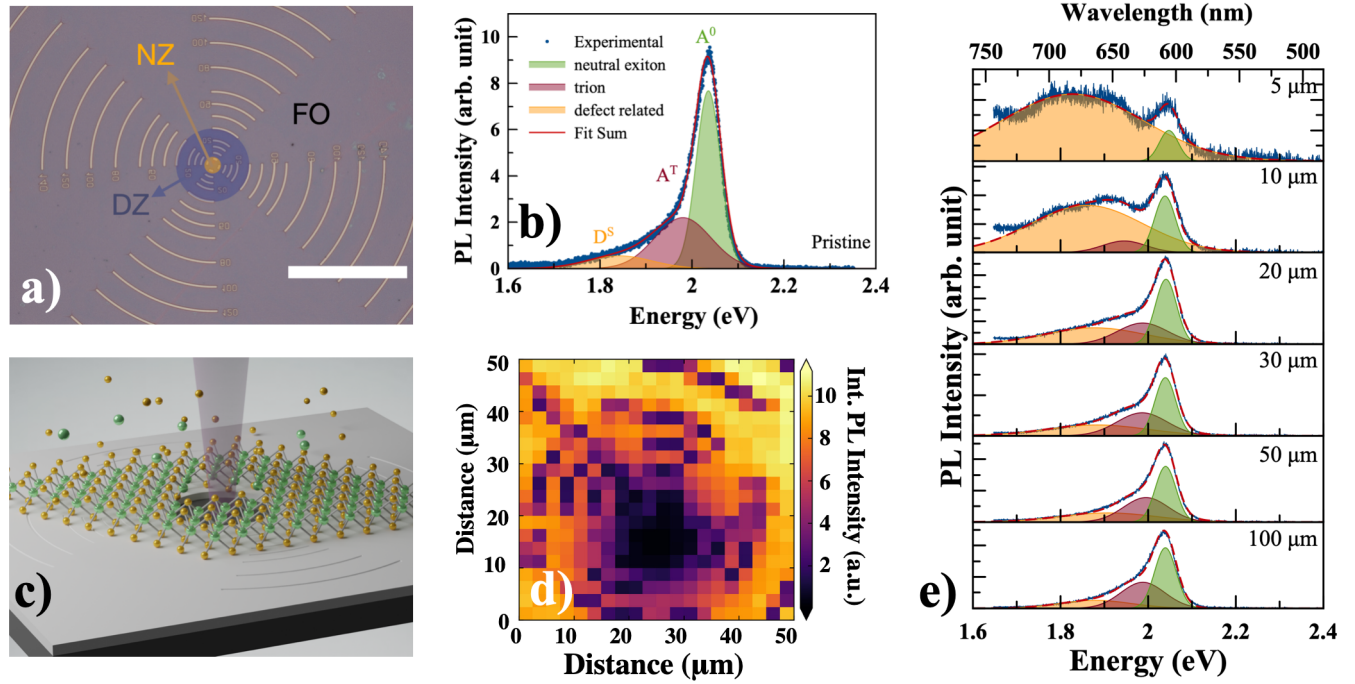


Figure 1. Steady-state photoluminescence from monolayer WS_2 samples. a) Optical microscope image of a wet-transferred ML WS_2 on a pre-patterned SiO_2/Si substrate, the scale bar is $100\ \mu\text{m}$; different colour shades in (a) indicate the three zones - we divide the sample into the near zone (NZ), the dark zone (DZ) and the far-out zone (FO). PL spectra of b) as-transferred ML WS_2 (referred to pristine) on a SiO_2/Si substrate, c) Schematic drawing of the FIB lithography process on a $\text{WS}_2/\text{SiO}_2/\text{Si}$ sample, d) PL mapping of a FIB-milled $\text{WS}_2/\text{SiO}_2/\text{Si}$ sample (Ga^+ beam current is $30\ \text{pA}$) and e) PL spectra at different locations, with the distance from the FIB milling position labelled on each spectrum. The green, red, and orange colours in (b and e) indicate the three emission peaks originated from neutral exciton (A^0), trion (A^T) and defect-state (D^S), respectively.

A hole with 2 μm in diameter and 50 nm in depth was milled on the $\text{WS}_2/\text{SiO}_2/\text{Si}$ sample using a dual-beam FIB-SEM system, with a constant dose of $333.4 \text{ pC}/\mu\text{m}^2$ (a volume-per-dose of $240 \text{ nm}^3/\text{nC}$). The lateral impact of the Ga^+ FIB process on the optical properties of large area ML WS_2 was investigated. Various Ga^+ beam currents in the range of 10-3000 pA were tested in the milling process. After the FIB milling process, we remeasured the PL, see Figure 1d and 1e. We divide the lateral area outside the milled hole into three zones: a “near” zone (0-5 μm radius around the milled hole, where 0 is the centre of the hole), a “dark” zone (further 5-30 μm radius away from the hole), and a “far-out” zone (beyond 30 μm from the hole). Figure 1e shows the evolution of the PL spectra moving from the “near” to “far” zone. The total PL intensity and the intensity of the neutral exciton peak (A^0) increase. In the “near” zone, the defect emission (D^S) dominates. It is obvious that although the milling area is only 1 μm in radius, the laterally affected area is remarkably larger, with a distance up to 30 μm . This extended damage range is caused by the deleterious tail of the ion beam, which consists of unfocused ions and ions in the residual gas in the vacuum system, resulting in the removal of atoms in the ML WS_2 and ion contamination on the ML surface.

To investigate the nature of the defect-bound emission D^S at 1.8 eV, we carried out Raman measurements. Figure 2a shows the Raman spectra of pristine and milled ML WS_2 . Several first and second-order characteristic peaks were observed in the ML WS_2 and marked in Figure 2a^{32,37,38}. At around 355 cm^{-1} , we observed a reduction in the peak intensity and a blue shift of this broad peak. Multi-peak fitting is employed to deconvolve this peak into two sub-peaks, at 349 and 357 cm^{-1} respectively, which correspond to the second-order longitudinal mode (2LA(M)) and in-plane vibrations of tungsten and sulphur atoms ($E_{2g}^1(\Gamma)$)^{32,37,38}. The lateral damage in ML WS_2 by the FIB milling process is evident by tracking the deconvolved 2LA(M) and $E_{2g}^1(\Gamma)$ peak intensities and widths at various lateral positions (see Figure 2c and 2d). While the peak position of the in-plane vibrations $E_{2g}^1(\Gamma)$ is not affected, the second-order longitudinal mode 2LA(M) is blue-shifted and suppressed around the milled area. This indicates an increased vacancies-phonon scattering within the 30 μm radius area (in the “near” and “dark” zones), due

to the higher density of both sulphur and tungsten vacancies created by the deleterious tail of the ion beam

39

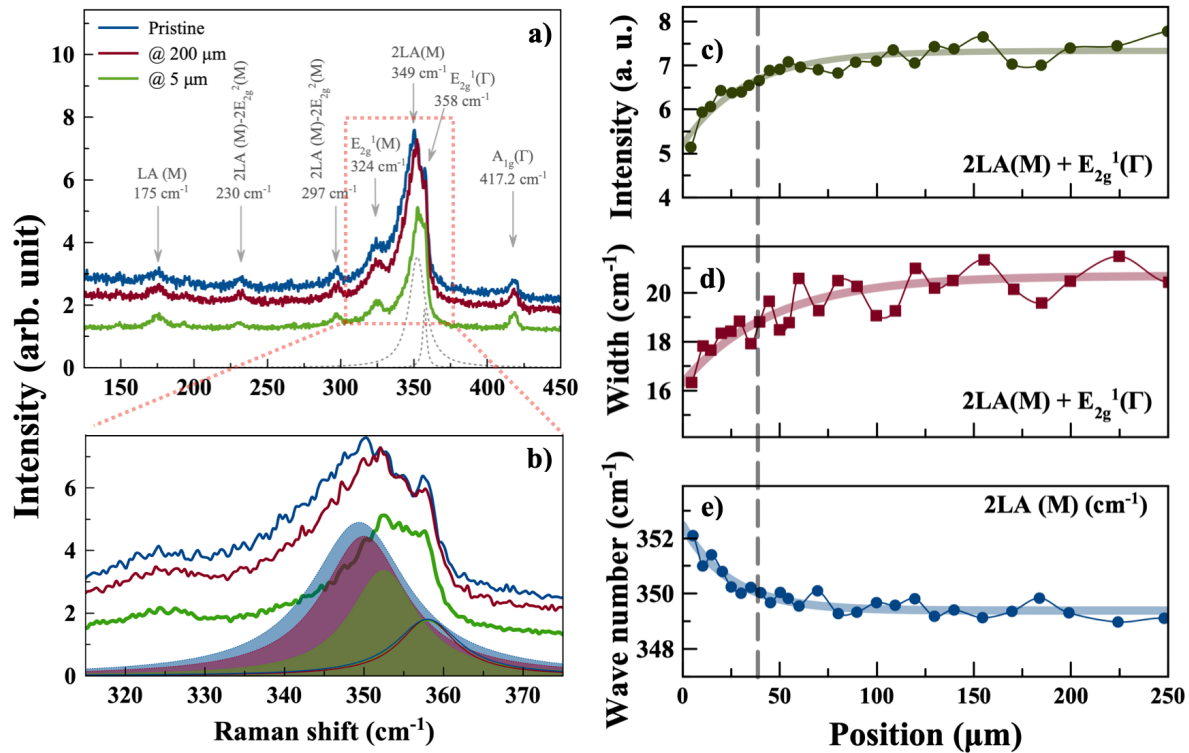


Figure 2. Raman spectroscopy. **a)** Raman spectra of pristine and FIB-milled ML WS₂ (5 and 200 μm away from the milled area); **b)** Raman peak around 355 cm⁻¹ deconvolved it into two peaks: 2LA (M) and E_{2g}¹(Γ); **c)** peak intensity, **d)** peak width (full width at half maximum, FWHM) and **e)** peak frequency of 2LA (M) as a function of lateral position.

We further investigated the ion beam damage mechanisms around the milled area by time- and spatially- resolved PL measurements, using a sample-scanning confocal fluorescence time-correlated single-photon counting (TCSPC) setup, shown in Figure 3a. The fluorescence lifetime and decay data are determined using TCSPC with emission detected on single-photon avalanche photodiodes, which are integrated with an inverted confocal microscope with a 100x oil-immersion objective (NA = 1.45). Excitation is provided by a 405 nm laser diode at a 40 MHz repetition rate. As clearly seen in the PL

mapping (Figure 3b), there is a ring of higher intensity fluorescence surrounding the milled hole. To help understand the origin of this bright ring in the near zone, we split the collected PL with a dichroic filter centred at 638 nm (being just between the trion and the defect-bound exciton peak wavelengths) to allow us to identify the collected photons at shorter and longer wavelengths simultaneously. With this configuration, we can produce a colour ratio for the PL images, which indicates the “ring” emission is primarily comprised of photons at shorter wavelengths (< 638 nm). Based on the wavelength information, the origin of this “ring” emission could be either neutral excitons or trions, or a combination of both. However, it is known that the trion-induced emission is slower than the neutral exciton emission^{40,41}. The time-resolved decay analysis confirms that the “ring” is mainly trion emission. The decay of the ring emission is significantly slower than the emission in the “far-out” zone, which is mainly neutral excitons (see Figure 3d and Table 1). Unlike the native defect and substrate-induced trions, we believe the “ring” originated via two possible routes: first, the positively charged Ga ions depositing and charging the monolayer observed via an electrostatic force microscope, and second, the free carriers accumulating on the edge forming more edge states, resulting in enhanced trion emission; similar effects have been observed in other TMDCs^{30,35,41,42}.

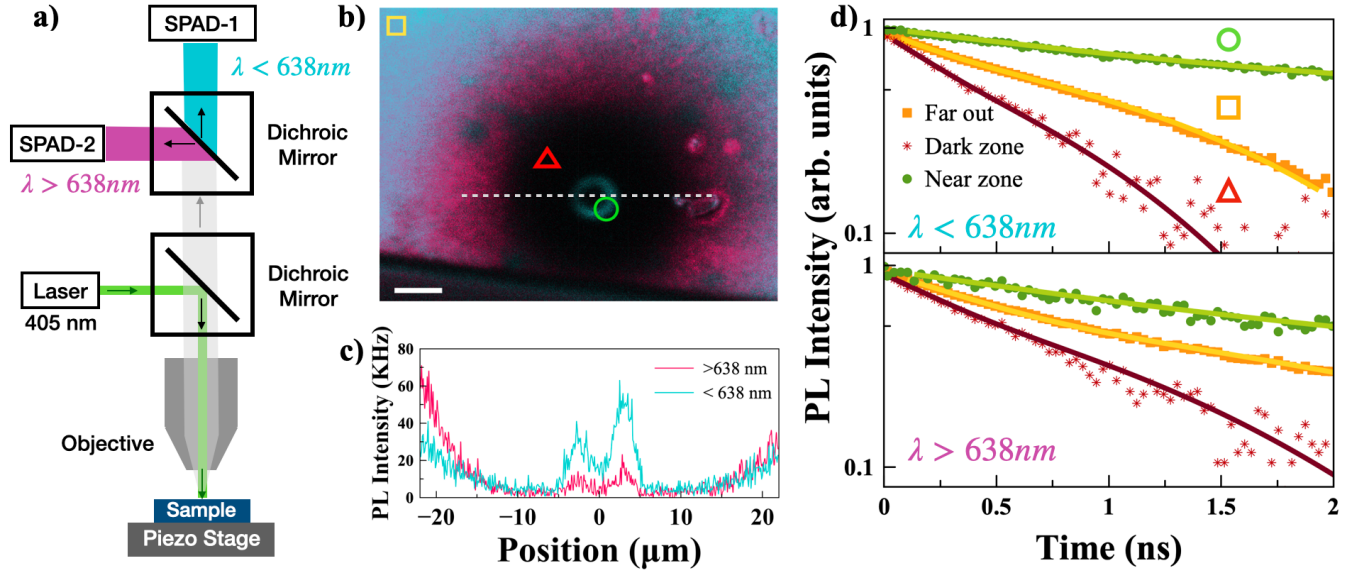


Figure 3. Time-resolved photoluminescence from FIB-milled ML WS₂. a) Experimental setup of the time-resolved fluorescence confocal microscope; b) PL mapping of a FIB-milled sample, with a scale bar of 10 μm ; c) PL intensity profile at positions along the dashed line in (b) as a function of lateral position, below (blue) and above (pink) 638 nm; d) the time-resolved decay curves at three locations for wavelengths below and above 638 nm: in the far-out zone (yellow squares), in the dark zone (red triangles), and on the “ring” (green circles).

Table 1. Exponential lifetimes, τ , and pre-exponential amplitudes (A) of the PL emissions at different locations, fitted with two exponential components

Wavelength		Far-out zone, τ	Dark zone, τ	Near zone Ring, τ
$\lambda > 638 \text{ nm}$	A1	187 ps (0.79)	149 ps (0.73)	552 ps (0.61)
	A2	905 ps (0.21)	539 ps (0.27)	2600 ps (0.39)
$\lambda < 638 \text{ nm}$	A1	140 ps (0.77)	120 ps (0.67)	586 ps (0.72)
	A2	429 ps (0.23)	392 ps (0.33)	3200 ps (0.28)

To gain a comprehensive understanding of the lateral damage in the extended area as a function of the ion beam current used, we performed the FIB milling process on ML WS₂ samples with a variety

of beam currents, from 10 pA to 3 nA. We observed the same trend in the samples milled with beam currents ranging from 10 up to 100 pA, i.e. a linear increase of PL moving away from the milling position in the dark zone, then reaching saturation in the far-out zone, as shown in the normalised PL intensity trend in Figure 4a. While the size of the short-range damage area (the dark zone) remains unaffected by the FIB processes, we observe a current-dependent total emission intensity in the far-out zone. The higher the ion beam current that is used, the less PL intensity is measured. Moreover, the FWHM of the PL spectrum is another indicator of the ion current-dependent damage in the far-out zone. As shown in Figure 4c, the FWHM of the PL spectrum broadens due to the increased defect-bound exciton emissions. It is evident that during the milling process, the ion-beam current plays a crucial role in the lateral damage effect on the ML WS₂, contrary to the studies carried out on graphene^{25,26}. This secondary far-range damage is due to sputtered Ga⁺. In a dual-beam-equipped FIB system, the sputtered Ga ions can spread to hundreds of μm away from the milled area. This has been experimentally observed using a time-of-flight secondary ion mass spectroscopy in a similar dual beam FIB⁴³. This wider range of ion-sputtering induces secondary damage as the Ga⁺ and milled atoms that are previously deposited on all the surfaces inside the vacuum chamber (such as the SEM column, the probes etc.) are redeposited on the ML WS₂. Redeposition of the Ga⁺ can be the main reason for the long-range lateral damage, and this can be eliminated by achieving a better vacuum in the chamber. Here, by using a lower beam current, the time required to mill the same amount of material is longer and thereby, it results in additional evacuation of the secondary sputtered ions from the surfaces and the residual gas in the chamber, leading to smaller overall damage of the ML WS₂. The Ga⁺ density on different samples milled with different ion beam currents measured by energy dispersive X-Ray spectroscopy, is noticeably different, as shown in Figure 4d. While only one type of Ga⁺ distribution (a sharp peak at the milling position) is observed on the low current samples, an additional wide-ranged Ga⁺ distribution is detected on the high current samples, which causes secondary damage to the TMDC MLs.

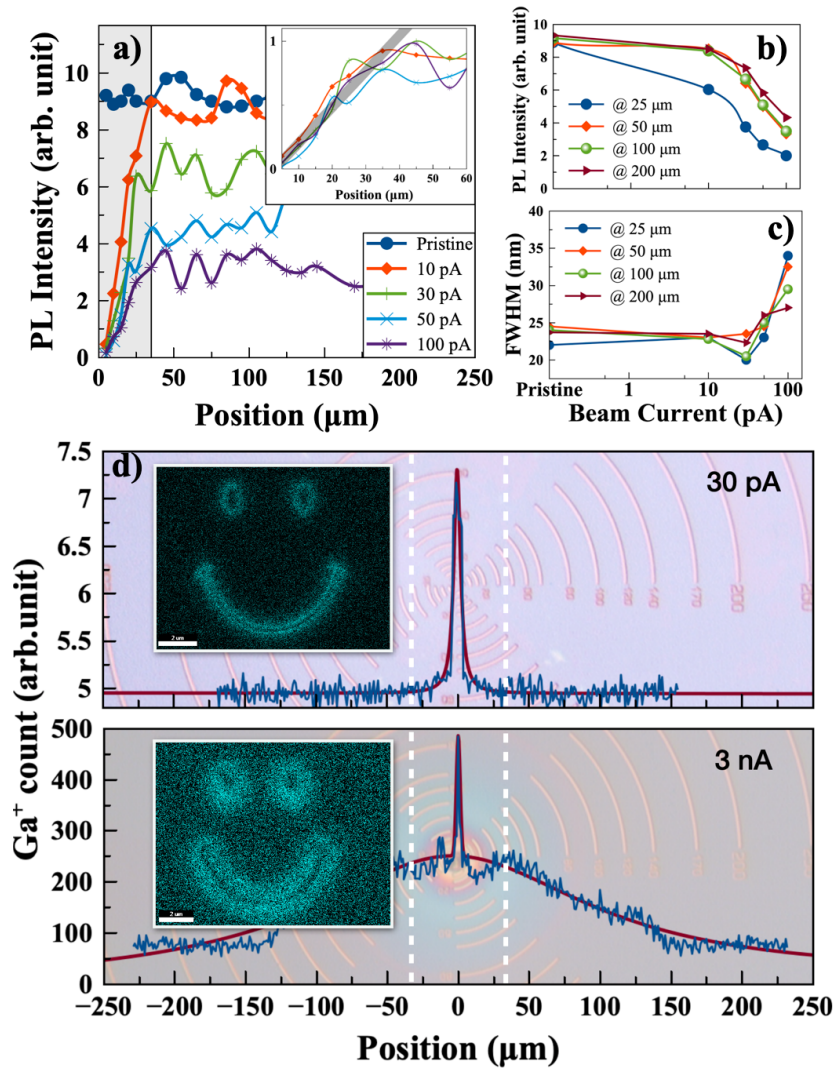


Figure 4. PL dependency on gallium ion beam current. **a)** The emission intensity of the neutral exciton as a function of position, with a range of ion beam current tested; inset is with the intensity normalised to the maximum value on each sample; **b)** Integrated PL intensity and **c)** FWHM of the PL spectra in the “dark” and “far-out” zone as a function of ion beam current. **d)** Distribution of Ga⁺ on the samples that the centre is milled with 30 pA and 3 nA ion beam current, respectively. We marked the edges of the “dark” zone with two dashed lines. Inset shows two energy dispersive X-Ray (EDX) mapping after a smiley face milled with the corresponding current. The scale bar is 2 μm.

In conclusion, here we have reported the lateral damage effects of a focused ion beam on a large-area CVD grown and transferred monolayer WS₂. Three distinct zones situated at different distances from the milling location were clearly identified and the distance-dependent damage mechanisms were explained. The main mechanism for short-range (radius of 0-30 μm) damage is the removal of tungsten and sulphur atoms in the monolayer by the primary ions and ion contaminants on the monolayer surface. The long-range (radius > 30 μm) damage originates from the redeposition of the secondary ions from the residual gas and the ion-electron beam column surfaces. The PL emission was significantly reduced, down to 10% in the short range, however, a bright ring-shaped feature, with half of the original emission intensity, was observed at the edge of the milled area. It is understood that the “ring” is mainly trion emission at a longer wavelength compared to the original emission, due to the charging effect from sputtered Ga⁺ deposition. This suggests the focused ion beam can be used to tailor the optical properties of TMDC monolayers. We also conclude that while the short-range damage is inevitable, the impact of the weak (secondary) damage can be avoided by reducing the ion beam current during the FIB process. These results pave the way for the use of heavy ion beam-based tools to fabricate novel optoelectrical devices based on the 2D TMDC materials, such as single-photon emitters, memory devices, resistors, and atomically thin circuits, on a wafer scale.

AUTHOR INFORMATION

Corresponding Author

* Fahrettin Sarcan: Department of Physics, Faculty of Science, Istanbul University, Vezneciler, 34134, Istanbul, Turkey, orcid.org/0000-0002-8860-4321, email: fahrettin.sarcan@istanbul.edu.tr

* Yue Wang: Department of Physics, University of York, Heslington, York, YO10 5DD, United Kingdom, orcid.org/0000-0002-2482-005X, email: yue.wang@york.ac.uk

Author Contributions

X.W., B.C. performed the WS₂ wafer growth for this project and the initial characterisation of the wafer, M.H. oversaw the scientific development of 2D material wafer-scale growth at AIXTRON. F.S. and Y.W. fabricated the samples, performed all the SEM-FIB, EDX, EFM measurements, and characterised the steady-state photoluminescence. N.J.F. and G.J.H. performed the time-resolved photoluminescence measurements. P.Z., T.S-M. and D.G. performed the Raman measurements. F.S., Y.W., T.F.K., N.J.F., G.J.H., P.Z., T.S-M., and D.G analysed the results. F.S. A.E., A.I.T., T.F.K., G.J.H. and Y.W. managed various aspects and funded the project. F.S. and Y.W. wrote the manuscript with contributions from all co-authors. Y.W. oversaw the entire project.

Funding Sources

Royal Academy of Engineering

Scientific Research Projects Coordination Unit of Istanbul University

The Scientific and Technological Research Council of Turkey

European Research Council

EPSRC

ACKNOWLEDGMENT

Y.W. acknowledges a Research Fellowship (TOAST) awarded by the Royal Academy of Engineering. F.S. gratefully acknowledges the support from the Scientific Research Projects Coordination Unit of Istanbul University (FUA-2018-32983) and The Scientific and Technological Research Council of Turkey (TUBITAK) project (121F169). P.Z., T.S-M., D.G. and A.I.T. acknowledge the European Graphene Flagship Project (881603) and EPSRC (EP/S030751/1 and EP/V006975/1). G.J.H. acknowledges EPSRC (EP/V004921/1 and EP/V048805/1). We would like to extend our

acknowledgements to a few colleagues at AIXTRON, Clifford McAleese, Sergej Pasko, Simonus Krotkus, for their contribution to WS₂ MOCVD growth development.

ABBREVIATIONS

TMDCs, Two-dimensional transition metal dichalcogenides; PL, photoluminescence; FIB, Focused ion beam; ML, monolayer; NZ; near zone, DZ; dark zone, FO; far-out zone, TCSPC; time-correlated single-photon counting, FWHM; full width at half maximum

REFERENCES

1. Liu, Q. *et al.* Sub-5 nm Lithography with Single GeV Heavy Ions Using Inorganic Resist. *Nano Lett* **21**, 2390–2396 (2021).
2. Hentschel, M., Karst, J. & Giessen, H. Tailored Optical Functionality by Combining Electron-Beam and Focused Gold-Ion Beam Lithography for Solid and Inverse Coupled Plasmonic Nanostructures. *Adv Opt Mater* **8**, 2000879 (2020).
3. Mendelson, N. *et al.* Coupling Spin Defects in a Layered Material to Nanoscale Plasmonic Cavities. *Adv Mater* **34**, 2106046 (2022).
4. Semple, M., Hryciw, A. C., Li, P., Flaim, E. & Iyer, A. K. Patterning of Complex, Nanometer-Scale Features in Wide-Area Gold Nanoplasmonic Structures Using Helium Focused Ion Beam Milling. *Acs Appl Mater Inter* **13**, 43209–43220 (2021).
5. Manoccio, M., Esposito, M., Passaseo, A., Cuscunà, M. & Tasco, V. Focused Ion Beam Processing for 3D Chiral Photonics Nanostructures. *Micromachines-basel* **12**, 6 (2020).
6. Graziosi, T., Mi, S., Kiss, M. & Quack, N. Single crystal diamond micro-disk resonators by focused ion beam milling. *Apl Photonics* **3**, 126101 (2018).
7. Lebedev, D. *et al.* Focused ion beam milling based formation of nanochannels in silicon-glass microfluidic chips for the study of ion transport. *Microfluid Nanofluid* **25**, 51 (2021).

8. Wang, Y. *et al.* Perovskite–Ion Beam Interactions: Toward Controllable Light Emission and Lasing. *Acs Appl Mater Inter* **11**, 15756–15763 (2019).
9. Jadwiszczak, J. *et al.* MoS₂ Memtransistors Fabricated by Localized Helium Ion Beam Irradiation. *Acs Nano* **13**, 14262–14273 (2019).
10. Li, W. *et al.* A Review of Recent Applications of Ion Beam Techniques on Nanomaterial Surface Modification: Design of Nanostructures and Energy Harvesting. *Small* **15**, 1901820 (2019).
11. Phan, H.-P. *et al.* Highly sensitive pressure sensors employing 3C-SiC nanowires fabricated on a free standing structure. *Mater Design* **156**, 16–21 (2018).
12. Li, P. *et al.* Recent advances in focused ion beam nanofabrication for nanostructures and devices: fundamentals and applications. *Nanoscale* **13**, 1529–1565 (2020).
13. Thiruraman, J. P. *et al.* Angstrom-Size Defect Creation and Ionic Transport through Pores in Single-Layer MoS₂. *Nano Lett* **18**, 1651–1659 (2018).
14. Qian, Q. *et al.* Defect creation in WSe₂ with a microsecond photoluminescence lifetime by focused ion beam irradiation. *Nanoscale* **12**, 2047–2056 (2019).
15. Ma, L. *et al.* Tailoring the optical properties of atomically-thin WS₂ via ion irradiation. *Nanoscale* **9**, 11027–11034 (2017).
16. Asaithambi, A. *et al.* Laser- and Ion-Induced Defect Engineering in WS₂ Monolayers. *Phys Status Solidi Rrl Rapid Res Lett* **15**, 2000466 (2021).
17. Chen, R. *et al.* Design of high performance MoS₂-based non-volatile memory via ion beam defect engineering. *2d Mater* **6**, 034002 (2019).
18. Heilmann, M., Deinhart, V., Tahraoui, A., Höflich, K. & Lopes, J. M. J. Spatially controlled epitaxial growth of 2D heterostructures via defect engineering using a focused He ion beam. *Npj 2d Mater Appl* **5**, 70 (2021).
19. Bui, M. N. *et al.* Low-energy Se ion implantation in MoS₂ monolayers. *Npj 2d Mater Appl* **6**, 42 (2022).
20. Stanford, M. G. *et al.* Focused helium-ion beam irradiation effects on electrical transport properties of few-layer WSe₂: enabling nanoscale direct write homo-junctions. *Sci Rep-uk* **6**, 27276 (2016).
21. Stanford, M. G. *et al.* High Conduction Hopping Behavior Induced in Transition Metal Dichalcogenides by Percolating Defect Networks: Toward Atomically Thin Circuits. *Adv Funct Mater* **27**, 1702829 (2017).

22. Fox, D. S. *et al.* Nanopatterning and Electrical Tuning of MoS₂ Layers with a Subnanometer Helium Ion Beam. *Nano Lett* **15**, 5307–5313 (2015).
23. Andersen, A. B., Shivayogimath, A., Booth, T., Kadkhodazadeh, S. & Hansen, T. W. Limiting Damage to 2D Materials during Focused Ion Beam Processing. *Phys Status Solidi B* **257**, 2000318 (2020).
24. Mupparapu, R. *et al.* Facile Resist-Free Nanopatterning of Monolayers of MoS₂ by Focused Ion-Beam Milling. *Adv Mater Interfaces* **7**, 2000858 (2020).
25. Liao, Z. *et al.* Lateral damage in graphene carved by high energy focused gallium ion beams. *Appl Phys Lett* **107**, 013108 (2015).
26. Thissen, N. F. W. *et al.* The effect of residual gas scattering on Ga ion beam patterning of graphene. *Appl Phys Lett* **107**, 213101 (2015).
27. Huang, M., Yan, H., Heinz, T. F. & Hone, J. Probing Strain-Induced Electronic Structure Change in Graphene by Raman Spectroscopy. *Nano Lett* **10**, 4074–4079 (2010).
28. Hang, S., Muktadir, Z. & Mizuta, H. Raman study of damage extent in graphene nanostructures carved by high energy helium ion beam. *Carbon* **72**, 233–241 (2014).
29. Fang, H. *et al.* 1305 nm Few-Layer MoTe₂-on-Silicon Laser-Like Emission. *Laser Photonics Rev* **12**, 1800015 (2018).
30. Kastl, C. *et al.* Effects of Defects on Band Structure and Excitons in WS₂ Revealed by Nanoscale Photoemission Spectroscopy. *Acs Nano* (2019) doi:10.1021/acsnano.8b06574.
31. Carozo, V. *et al.* Optical identification of sulfur vacancies: Bound excitons at the edges of monolayer tungsten disulfide. *Sci Adv* **3**, e1602813 (2017).
32. Plechinger, G. *et al.* Identification of excitons, trions and biexcitons in single-layer WS₂. *Phys Status Solidi Rrl - Rapid Res Lett* **9**, 457–461 (2015).
33. Chow, P. K. *et al.* Defect-Induced Photoluminescence in Monolayer Semiconducting Transition Metal Dichalcogenides. *Acs Nano* **9**, 1520–1527 (2015).
34. Sebait, R., Biswas, C., Song, B., Seo, C. & Lee, Y. H. Identifying Defect-Induced Trion in Monolayer WS₂ via Carrier Screening Engineering. *Acs Nano* **15**, 2849–2857 (2021).
35. Drüppel, M., Deilmann, T., Krüger, P. & Rohlfing, M. Diversity of trion states and substrate effects in the optical properties of an MoS₂ monolayer. *Nat Commun* **8**, 2117 (2017).
36. Tongay, S. *et al.* Defects activated photoluminescence in two-dimensional semiconductors: interplay between bound, charged and free excitons. *Sci Rep-uk* **3**, 2657 (2013).

37. Zhao, W. *et al.* Lattice dynamics in mono- and few-layer sheets of WS₂ and WSe₂. *Nanoscale* **5**, 9677–9683 (2013).
38. Zobeiri, H. *et al.* Effect of temperature on Raman intensity of nm-thick WS₂: combined effects of resonance Raman, optical properties, and interface optical interference. *Nanoscale* **12**, 6064–6078 (2020).
39. Xie, G. *et al.* A Bond-order Theory on the Phonon Scattering by Vacancies in Two-dimensional Materials. *Sci Rep-uk* **4**, 5085 (2014).
40. Godde, T. *et al.* Exciton and trion dynamics in atomically thin MoSe₂ and WSe₂: Effect of localization. *Phys Rev B* **94**, 165301 (2016).
41. Goswami, T., Rani, R., Hazra, K. S. & Ghosh, H. N. Ultrafast Carrier Dynamics of the Exciton and Trion in MoS₂ Monolayers Followed by Dissociation Dynamics in Au@MoS₂ 2D Heterointerfaces. *J Phys Chem Lett* **10**, 3057–3063 (2019).
42. Su, W., Dou, H., Huo, D., Dai, N. & Yang, L. Enhancing photoluminescence of trion in single-layer MoS₂ using p-type aromatic molecules. *Chem Phys Lett* **635**, 40–44 (2015).
43. Bender, H. *et al.* Surface contamination and electrical damage by focused ion beam: conditions applicable to the extraction of TEM lamellae from nanoelectronic devices. *Semicond Sci Tech* **30**, 114015 (2015).